The GraF instrument for imaging spectroscopy with the adaptive optics[†]

A. Chalabaev, E. le Coarer, P. Rabou, Y. Magnard and P. Petmezakis
Laboratoire d'Astrophysique, Observatoire de Grenoble, UMR 5571, CNRS and Université Joseph Fourier, B.P. 53X, F-38041 Grenoble, France

D. Le Mignant
W. M. Keck Observatory, 65-1120 Mamalahoa Highway, Kamuela HI96743, U.S.A.

Abstract. The GraF instrument using a Fabry-Perot interferometer cross-dispersed with a grating was one of the first integral-field and long-slit spectrographs built for and used with an adaptive optics system. We describe its concept, design, optimal observational procedures and the measured performances. The instrument was used in 1997-2001 at the ESO 3.6 m telescope equipped with ADONIS adaptive optics and SHARPII+ camera. The operating spectral range was 1.2-2.5 μm. We used the spectral resolution from 500 to 10 000 combined with the angular resolution of $0.1''$-$0.2''$. The quality of GraF data is illustrated by the integral field spectroscopy of the complex $0.9'' \times 0.9''$ central region of η Car in the 1.7 μm spectral range at the limit of spectral and angular resolutions.

1. Introduction

High angular resolution observations at the diffraction limit of the ground based large telescopes were pioneered using the speckle analysis of images (Labeyrie, 1970), however their sensitivity was severely limited by the necessity to keep exposures short in order to "freeze" the turbulence induced patterns. The adaptive optics overcame this obstacle allowing long exposures (COME-ON and ADONIS at the ESO 3.6 m telescope, Beuzit et al., 1997, PUEO at the CFHT, Rigaut et al., 1998, NAOS at the ESO VLT, Lagrange et al., 2003, and others). The limiting magnitude on the telescopes equipped with the adaptive optics (hereafter AO) is now defined by the detector and optics efficiency as for any observations, while the angular resolution is close, at least in the IR, to the telescope diffraction limit, about $0.1''$ for a 4 m aperture at $\lambda = 2\,\mu m$.

The achievements of the AO were firstly exploited for imaging (see reviews by Close, 2000, Lai, 2000, Menard et al., 2000). The next step

---

[†] Based on observations collected at European Southern Observatory, Chile, La Silla 3.6 m telescope, ESO period 59, technical time.

was to use the adaptive optics for spectroscopy. Indeed, the combination of high angular and high spectral resolutions is a key issue for a number of observational programmes such as physics and evolution of multiple stellar systems, morphology and dynamics of circumstellar gas and jets in young and evolved stars, etc.

Driven by this ideas, the GraF project was started in 1995 with the aim to build an imaging spectrograph optimized for the use with the ADONIS at the ESO 3.6 m telescope. The instrument is based on the integral field spectroscopic properties of the Fabry-Perot interferometer (hereafter FPI) used in cross-dispersion with a grating (le Coarer et al., 1992, 1993). It was tested at the telescope in 1997 and successfully used for a number of astronomical programmes in 1998-2001 (for preliminary results see Chalabaev et al., 1999a, 1999b, 1999c, Trouboul et al., 1999).

In the present article we describe in details the optical concept and the instrument built to fit the constraints imposed by ADONIS (Beuzit et al., 1997) and the SHARPII+ camera (Hofmann et al., 1995). We give the account of the observational procedures emerged from our experience as optimal, present the measured performances, and illustrate them by a sample of reduced data obtained at the limit of the instrument possibilities in terms of the angular and spectral resolutions.

The discussion will be restricted to the applications of a high spectral resolution ($R \simeq 5000 \text{-} 10000$) in a moderate passband ($\Delta\lambda \leq 50$) combined with a high angular resolution ($\simeq 0.1'' \text{-} 0.2''$) in a small field of view ($FOV \leq 15''$). The operating spectral range of the instrument was $1.2 - 2.5 \ \mu m$.

We hope that this one of the first experiences of the imaging spectroscopy with the adaptive optics (see also Bacon et al., 1995, Lavalley et al., 1997) will be useful for designers and users of future spectro-imaging instruments combining the high angular and high spectral resolutions.

2. Image restoration aspects

Let us in what follows to make the emphasis of the discussion on the scarcely resolved objects, i.e. having the spatial[1] spectrum in the Fourier domain comparable in the extent to that of the AO corrected telescope modulation transfer function (MTF).

There are two reasons for such a choice. Firstly, as witnessed by the reviewers (cf. Close, 2000, Lai, 2000, Menard et al., 2000), the AO provides a considerable scientific contribution mainly in the case where

---

[1] We will say indifferently "spatial" and "angular", the corresponding variables on the celestial sphere being related by a simple scaling factor.

the object under study, having remained point-like at lesser angular resolutions, becomes scarcely resolved, revealing new spatial features.

The second reason is dictated simply by the fact that the scarcely resolved objects are the most difficult to measure, so that the overall performance of a new instrument at the limit of resolution is best evaluated on such objects.

We can already note that the importance of the scarcely resolved objects shapes the specifications on the AO assisted spectrograph. Indeed, to recover the information up to the highest possible spatial frequency implies the image restoration, and this aspect has necessarily to be taken into account in the design of the spectrograph.

2.1. GENERAL

We shall consider the flux density distribution $S(x, y, \lambda)$ which is non-zero at least at 2 points of the two-dimensional (2D) sky field $\{x, y\}$. Here, x and y are the spatial coordinates, and λ is the wavelength. As it was already said in Sect. 1, the discussion will be restricted to small fields, $\leq 15''$.

The image restoration problem of imaging spectroscopy in the general case consists in finding the best estimate $\hat{S}(x, y, \lambda)$ of the object flux distribution density $S(x, y, \lambda)$, satisfying the tri-dimensional integral equation of convolution:

$$F(x, y, \lambda) = \int\int\int d\xi\, d\zeta\, dw \cdot S(\xi, \zeta, w) \cdot \mathcal{G}(\xi - x, \zeta - y, w - \lambda) \quad (1)$$

where F is the measured flux density distribution and $\mathcal{G}$ is the instrumental impulse response.

The solution of the integral equation of convolution is known to be unstable (Turchin et al., 1971; see also Lucy, 1994a). The calibration errors of $\mathcal{G}$ are strongly amplified in the final result of image restoration, in particular at high frequencies, so that the solution $\hat{S}$ has to be regularized, i.e. searched in a space of appropriate smooth functions (see for details Tikhonov and Arsenin, 1977, Titterington, 1985, Lucy, 1994b).

The image restoration can be carried out using either one of the many proposed deconvolution algorithms (e.g. Cornwell, 1992, Magain et al., 1998, Lucy and Walsh, 2003, and references therein), or by modeling $\hat{S}$ from *a priori* defined physical considerations and then searching for the best fit of the convolution product $\hat{S} \otimes \mathcal{G}$ to F within the physical model.

It is clear that whatever the method adopted for the image restoration, the accurate calibration of $\mathcal{G}$ is of high importance. Let us analyze

the sources of the calibrations errors in the case of imaging spectroscopy in order to get guidelines of the instrumental concept.

2.2. Calibration errors

Firstly, we can simplify the Eq.(1) by noting that for the considered here angular fields, spectral passbands and resolutions (see Sect. 1) the 3D impulse response $\mathcal{G}$ can be written as the product of the spatial point-spread function (psf) $\mathcal{P}(x, y | \xi, \zeta; \lambda)$ and the instrumental spectral profile $\mathcal{L}(x, y; \lambda | w)$ (see e.g. Perina, 1971, Goodman, 1968, Mariotti, 1988). Then we get:

$$F(x, y, \lambda) = \int dw \cdot \mathcal{L}(x, y, \lambda - w) \int\int d\xi d\zeta \cdot S(\xi, \zeta, w) \cdot \mathcal{P}(\xi - x, \zeta - y, \lambda) \quad (2)$$

We will further assume that the relevant scientific information can be extracted without deconvolution on λ. In other words, we will limit the discussion to the frequently encountered case where the instrumental spectral profile $\mathcal{L}$ is much narrower than the studied spectral lines.

We can then write:

$$\mathcal{L}(x, y, \lambda - w) \simeq L(x, y, \lambda) \cdot \delta(\lambda - w) \quad (3)$$

where $L(x, y, \lambda)$ is the spectral transmission, a simple multiplicative factor, and $\delta(\lambda - w)$ is the Dirac impulse function.

The convolution concerns now only the spatial dimensions, so that the Eq.(2) is further simplified as follows:

$$F(x, y, \lambda) = L(x, y, \lambda) \int\int d\xi d\zeta \cdot S(\xi, \zeta, \lambda) \cdot \mathcal{P}(\xi - x, \zeta - y, \lambda) \quad (4)$$

The important consequence is that in the absence of the deconvolution on λ the contribution of the calibration errors on $\mathcal{L}$ to the uncertainty of the final estimate $\hat{S}$ is considerably reduced.

Furthermore, we note that usually the variations of $\mathcal{L}$ during observations are due to mechanical flexure at the telescope. They are slow, with the time scale of tens of minutes, and can be monitored with a good accuracy. Similarly, the dependence of $\mathcal{L}$ on x and y is stable and can be calibrated accurately.

In contrast to the relative stability of $\mathcal{L}$, the psf $\mathcal{P}$ undergoes significant temporal variations on the time scale of minutes or even shorter due to atmospheric turbulence. Although the AO improves dramatically the situation, the residual wavefront variations can still be significant. Their amplitude depends on the operating wavelength, the amplitude and the time scale of the atmospheric turbulence, the performances of the AO system and the telescope aperture size. With the

ESO 3.6 m telescope and the ADONIS, the variations of $\mathcal{P}$ expressed in terms of the Strehl ratio were found to change from 10 to 35 in the K band for the seeing value of $\approx 1.5''$ within the time interval of $10\,s$ (Le Mignant et al., 1999). The variability is *a fortiori* stronger at the shorter wavelengths of J and H bands.

As to the wavelength dependence of $\mathcal{P}$, it is negligible within the considered here spectral range of a single instrument setting, $\Delta\lambda/\lambda \leq 50$.

We can conclude that the main source of errors in the final result of image restoration, the flux distribution estimate $\hat{S}$, comes from the calibration of the spatial psf $\mathcal{P}$ due to its rapid variability. The way it is calibrated needs thus special attention. For instance, the calibration errors can be substantially reduced if $\mathcal{P}$ is measured simultaneously with the measurement of F, e.g. on a suitable source in the same field. If $\mathcal{P}$ can be measured only on a source off the field, it must be done as close in time as possible. The instrumental concept has to take into account these observational aspects.

It also appears important that the two-dimensional $\{x, y\}$-structure of the field and of the psf $\mathcal{P}$ is recorded with no scanning[2] on $\{x, y\}$, in order to keep the error on $\mathcal{P}$ homogeneous over x and y, thus avoiding a random scrambling of spatial features, which can be unrecoverable.

As to the spectral response $\mathcal{L}$, the contribution of its calibration errors in the final uncertainty on $\hat{S}$ is considerably lesser than that of $\mathcal{P}$. Indeed, the instrumental spectral profile $\mathcal{L}$ is relatively stable and can be calibrated much more accurately than $\mathcal{P}$. Furthermore, if no deconvolution is justified on λ, i.e. if the spectral resolutions high enough, then the error on $\mathcal{L}$ propagates into the error on $\hat{S}$ without amplification.

2.3. IMPLICATIONS FOR THE AO ASSISTED SPECTROSCOPY

The above given analysis provides the guidelines of the instrumental concept for the AO assisted imaging spectroscopy which can be briefly summarized as follows: (i) the calibration of the psf $\mathcal{P}$ has to be simultaneous, or as close in time as possible, to the measurement of the flux distribution F; (ii) the scanning over the spatial x- and y-axes must be avoided; (iii) if scanning is unavoidable due to the volume of data to be recorded, the instrument concept allowing λ-scanning is preferable.

Obviously, the ideal spectro-imaging instrument would record the entire cube of data $F(x, y, \lambda)$ in one single exposure with no scanning,

---

[2] We restrict the term of scanning to the recording data point after point, or line after line, distinguishing it from the mosaicing, i.e. recording a subregion by a subregion.

satisfying the criteria of both the accurate image restoration and the saving the telescope time.

The work is in progress on the "3D detectors" able to record both the position x, y and the energy λ of the photons, *cf.* the superconducting tunnel junctions (Perryman et al., 1994, Rando et al., 2000) or the dye-doped polymers (Keller et al., 1995). However, their sensitivity is still less convincing than that of the modern 2D-detectors.

The best available today solutions are offered by the optical set-ups known as the integral field spectrographs (IFS, Courtes, 1982, Bacon et al., 1995, Weitzel et al., 1994, Le Fevre et al., 1998, Eisenhauer et al., 2000). They use the 2D detectors to record $F(x, y, \lambda)$ with no scanning, provided the detector size is large enough to record the 3D data cube at once.

3.   Particular case of a "linear image"

Let us also consider the simplest case of the imaging spectroscopy when the object flux density $S(x, y, \lambda)$ is non-zero along a straight line, so that S is a function of only two variables, $S(x, \lambda)$.

In this "linear" case, frequently encountered in the astrophysical practice (e.g. binary stellar systems), the common grating spectrographs recording $F(x, \lambda)$ at a single setting offer a suitable solution, insuring the calibration of psf $\mathcal{P}$ homogeneous over the studied field $\{x\}$. Furthermore, in the case of a circumstellar nebular object, when the extended feature is a gas emitting only in spectral lines, the emission in the continuum corresponds to the point-like star and provides the calibration of $\mathcal{P}(x)$ simultaneous to the measurement of F.

4.   The minimum 3D data cube volume

At high angular and high spectral resolutions, the volume of data to be recorded in one observation of imaging spectroscopy can be large. Let us to estimate what is its minimum under typical astrophysical specifications.

Empirically, the angular field of $\simeq 3'' \times 3''$ would be adequate to study most types of objects of interest of the stellar physics. The pixel size of $0.05''$ is fixed by the angular resolution, which is $\approx 0.1''$ at a 4 m telescope at $\lambda = 2\,\mu$m. Thus, the record of the spatial flux distribution at a given wavelength $F_\lambda(x, y)$ consists of $60 \times 60 = 3600$ data values. Along the λ-axis, the minimum of about 100 points is suitable in order to record the profile of a spectral line and the adjacent continuum.
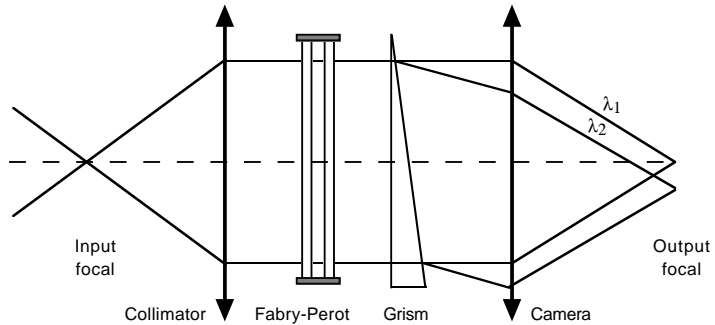
Figure 1. The optical concept of the the imaging spectrograph using a Fabry-Perot interferometer in cross-dispersion with a grating, replaced here by a grism for the convenience of the drawing.

Thus, the entire cube data volume is at least $60 \times 60 \times 100 \simeq 600^2$ values.

This largely exceeds the 256^2 size of the detector available with ADONIS/SHARPII+. In our case the IFS approach is clearly unaffordable, the scanning is imposed. Then, in agreement with the conclusions of error analysis in imaging spectroscopy given in Sect. 2.3, we adopted the concept of the λ-scanning imaging spectrograph described below.

5. The GraF concept

5.1. Optical scheme. Data cube structure

The concept uses a Fabry-Perot interferometer in cross-dispersion with a grating (hence the acronym we gave for this concept, GraF = **Gra**(*ting*) and **F**(*abry-Perot*). The set-up (see Fig. 1) was first described by Fabry (1905), and used for spectroscopy by Chabal and Pelletier (1965) and Kulagin (1980). The IFS property of the set-up was noticed by le Coarer (1992) and demonstrated by le Coarer et al. (1992, 1993). Baldry and Bland-Hawthorn (2000) went further, describing a tunable echelle imager, where a FPI is cross-dispersed with a grism and with an echelle grating.

In a single frame, GraF records the quasi-monochromatic images of the field $F_\lambda(x, y)$ corresponding to several values of λ, which is the distinctive property of an IFS instrument. The spectrum is sampled by a comb of the FPI transmission peaks (interference orders) separated by the interorder wavelength spacing $\Delta\lambda_f$ (Sect. 6). The whole set of λ values is recovered by scanning.

The structure of the spectro-imaging data cube is illustrated in Fig. 2. The FPI acts as a "multi-passband" filter. The light of different

FPI orders is sorted by the grating according their wavelength. The resulting series of quasi-monochromatic images of the sky field is formed in the output focal plane. Note that the width[3] of the entrance field must be limited by a focal aperture to avoid superposition of order images.

Anticipating a detailed discussion (Sect. 6), let us give the figures of a typical cube volume recorded with the actually built instrument. At each step of scanning, the detector frame of 256^2 pixels records 8 narrow-band images corresponding to the dispersed sequence of the FPI orders as selected by the grating angle value. Each FPI "order image" covers the same $1.5'' \times 12.4''$ region of the entrance sky field sampled with the pixels of $0.05''$, which makes $\simeq 30 \times 250 = 7440$ spatial pixels.

This is close to the estimated minimum required by the stellar observations, although, the width of the FOV $\simeq 1.5''$ is a factor of 2 less than the desirable $\simeq 3''$ value. For the observations of the elongated objects, this shortage is partially compensated by the considerable height of the FOV of $\simeq 12''$, which can be suitably aligned.

The spectral band covered by the detector is about 40 nm at $\lambda = 2.2$ μm, corresponding to 8 FPI orders. It is scanned in 48 FPI channel frames[4], although in special cases one can limit the scan to a narrower range of interest. The number of spectral samples in a full FPI scan is $48 \times 8 = 384$. The spectral passband of an image is $\delta\lambda \simeq 0.3\,\mathrm{nm}$ at $\lambda = 2\,\mu m$, so that the corresponding spectral resolving power is $R = \lambda/\delta\lambda \simeq 7000$. The total volume of the cube is $48 \times 256^2 = 3.15 \cdot 10^6$ pixels, or $\simeq 1770^2$ pixels.

5.2. Advantages and limitations of the concept

The GraF λ-scanning IFS appears as a suitable solution when scanning is imposed by the modest detector size. It allows a simultaneous record of several monochromatic images of a reasonably large field thus keeping possible an accurate image restoration.

Scanning is done by the comb of spaced FPI transmission peaks rather than by a contiguous set of the wavelength values like in a grating based instrument. The peaks spacing makes more certain to have in each frame at least one "order" image placed at the wavelengths of the continuum emission, thus providing a reference signal

---

[3] As in the slit spectroscopy, the width and the height are respectively the directions along and across the grating dispersion. At the same time, these directions correspond to the spatial axes which will be denoted hereafter as respectively x- and y-axes.

[4] The spectral step between FPI samples, h, is smaller than $FWHM/2$ often quoted as the "Nyquist" sampling. We will comment on this issue in Sect. 6.1.
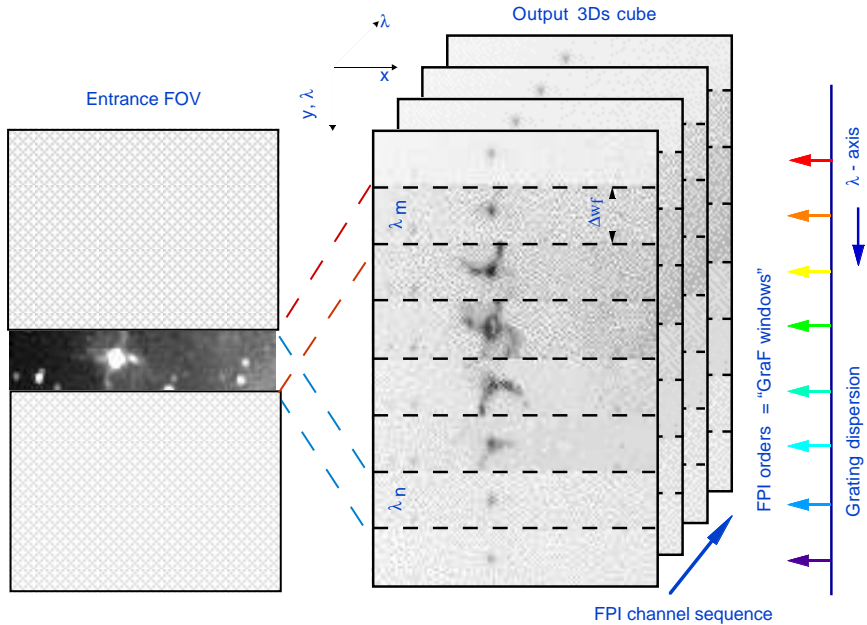
Figure 2. The structure of the GraF IFS cube. *Left*: The "Southern Crab" planetary nebula as it appears in the white light (simulated). The field of view is limited by a rectangular entrance aperture. *Right*: The images of the nebula in the light of a atomic spectral line (simulated image) as they appear in the focal plane of the GraF instrument. Each frame consists of several monochromatic "windows" corresponding to the FPI orders. Due to the differential motion of the nebulae, the aspect of the nebula is changing from one "window" to another.

for photometric monitoring and, in the nebular cases, the calibration of the $\mathcal{P}$ simultaneous to the measurement of F.

Another convenient point of the concept is the simplicity of transforming a grating spectrograph into a GraF instrument by adding solely a FPI and an adjustable slit (see also comments by Baldry and Bland-Hawthorn, 2000). *Vice versa*, the instrument is easily switched to a grating spectrograph for observations of "linear" objects.

However, the GraF concept is intrinsically scanning, so that if scanning is unnecessary, the GraF is slower than other mentioned above IFS concepts.

Further, the width of the FOV has an upper limit. Expressed in the elements of the angular resolution $\delta\phi$, the FOV width cannot exceed the FPI finesse value $\mathcal{F}$ (see Sect. 6.2). For the maximum $\mathcal{F}$ of $\simeq 40$ still suitable for the high-throughput imaging (Bland-Hawthorn, 1995), the maximum FOV width of a GraF is $\simeq 4''$ for $\delta\phi \simeq 0.1''$.

6. Formulae for GraF optical parameters

6.1. FPI formulae

Let us remind the basic terms describing the FPI properties. The FPI spectral transmission is a comb of peaks, called "orders", occurring at λ_m defined by the condition of the interference:

$$m\lambda_m = 2ne\cos i \tag{5}$$

where the integer m is the order of the interference, n the refractive index, e the gap between the FPI plates, and i the angle of incidence.

The value of λ_m varies over the FOV according to the value of i. However, as it can be estimated from Eq. 5, this variation is negligible: $\delta\lambda/\lambda \simeq 5\cdot10^{-9}$ for the considered fields of view $\leq 15''$. In what follows, it will be assumed that $i = 90°$, so that the gap e defines completely the set of λ_m.

The distance between two neighbor orders is called the interorder spectral spacing. Expressed in the wavelength units, $\Delta\lambda_f$, it can be written from Eq. 5 as follows:

$$\Delta\lambda_f = \frac{\lambda_m\lambda_{m+1}}{2ne} \simeq \frac{\lambda^2}{2ne} \tag{6}$$

It is often more convenient to use the interorder spacing expressed in the wavenumber units $\Delta\sigma_f$, which has no spectral dependence:

$$\Delta\sigma_f = \frac{1}{2ne} \tag{7}$$

The element of spectral resolution $\delta\lambda$ will be defined as the $FWHM$ of the instrumental profile $\mathcal{L}$. It has the advantage to be immediately measurable (see however Jones et al., 1995 for different criteria of resolution).

The effective finesse $\mathcal{F}$ is defined as the ratio of the interorder spectral spacing to the element of spectral resolution:

$$\mathcal{F} = \frac{\Delta\lambda_f}{\delta\lambda} \tag{8}$$

The instrumental profile $\mathcal{L}$ is the Airy function:

$$\mathcal{L} = \frac{1}{1 + \mathcal{F}sin^2(\pi\sigma/\Delta\sigma_f} \tag{9}$$

For high values of $\mathcal{F}$, it can be approximated by the Lorentzian:

$$\mathcal{L} = \frac{1}{1 + (2\sigma/\delta\sigma)^2} \tag{10}$$

Using Eqs.(6) and (8), the spectral resolving power $R = \lambda/\delta\lambda$ can be formally written as follows:

$$R = \frac{2ne\mathcal{F}}{\lambda} \qquad (11)$$

Given that the finesse $\mathcal{F}$ approximately corresponds to the number of the effective reflections on the FPI plates, the maximum optical path difference between the interfering wavefronts OPD_{max} can be written as follows:

$$OPD_{max} \approx 2ne\mathcal{F} \qquad (12)$$

The sampling step we used for the FPI scanning is $h = \delta\lambda/2.7$. This appears as "oversampling" as compared to the "canonic" value of $h_s \simeq 2$.

There are two ways to justify the used value of h. The first one is to argue that the Airy profile of $\mathcal{L}$ has a considerably sharper core than the more familiar Gaussian or $sinc^2$ profiles of grating spectrographs, so that the rate based on the convention $\delta\lambda = FWHM$ would certainly undersample the core profile.

More strictly speaking, let us recall that the step h allowing to fully interpolate the function with a finite Fourier spectrum must be $h \leq h_s = 1/(2 \cdot f_{cut})$ (Shannon theorem), where f_{cut} is the cut-off frequency of the Fourier spectrum. It happens that for a Gaussian profile, $\delta\lambda = FWHM \simeq 1/f_{cut}$, which conveniently translates into "the rule" $h_s = \frac{1}{2}\delta\lambda$. The trouble with FPI is that the Fourier transform of $\mathcal{L}$ is never zero[5] and has no f_{cut}. Thus, formally FPI escapes the Shannon theorem.

In practice, the effective number of reflexions on the FPI plates, hence the effective finesse $\mathcal{F}$ and the effective OPD_{max}, is limited by the noise, so that f_{cut} can be defined on this basis. For the same instrument, it will vary depending on the S/N ratio. The uncertainty on f_{cut}, and hence on h_s, explains the choice of a conservatively small value of $h = \delta\lambda/2.7$.

6.2. GraF formulae. The limits and optimum for the FOV width

In the absence of the grating, the output image would be a superposition of all images transmitted in the passbands of the FPI orders. The grating deviates each order light into a specific angle according to its wavelength λ_m, and thus spatially sorts the order images (see Fig. 2).

In the output focal plane, the shift between the order images Δw_f is equal to the interorder spectral spacing $\Delta\lambda_f$ scaled by the reciprocal

---

[5] *cf.* the Fourier transform of a Lorentzian is $exp(-\delta\sigma\pi f)$.

dispersion $rdisp$ (expressed in nm/pix) as follows:

$$\Delta w_f \ \ [pix] = \frac{\Delta\lambda_f}{rdisp} \qquad (13)$$

Since the axis of λ in the output focal plane is collinear with the spatial y-axis, the value of Δw_f can be also expressed in *arcsec* through the platescale H:

$$\Delta w_f \ \ [arcsec] = P \cdot \frac{\Delta\lambda_f}{rdisp} \qquad (14)$$

Albeit shifted according their wavelength, the order images superimpose. The confusion is finally avoided by limiting the width of the entrance FOV to the value Δw_f. The latter, expressed in *arcsec*, is the confusion free width of the FOV, or simply the free width (see Fig. 2).

The Eq.(13) seems to indicate that the free width Δw_f can be increased arbitrarily by increasing the grating spectral dispersion. However, the extension of the output psf along the λ-axis, measured as the FWHM $\delta\phi_{graf,disp}$, also increases with the dispersion due to collinearity of λ- and y axes.

We can write:

$$\mathcal{P}_{graf,disp} = \int dw \cdot (M_{FP}(w) \cdot \mathcal{P}_{ao}(w))\mathcal{L}_{gr}(w - \lambda) \qquad (15)$$

where $\mathcal{P}_{graf,disp}$ is the psf profile along the λ-axis at the GraF output, $\mathcal{P}_{ao}(\lambda)$ is profile of the monochromatic psf at the output of the adaptive optics, M_{FPI} is the spectral transmission of the FPI, and $\mathcal{L}_{gr}(w - \lambda)$ is the instrumental spectral profile of the grating.

For the corresponding FWHM's, we get :

$$\delta\phi_{graf,disp} \ \ [pix] \simeq \sqrt{\delta\phi_{ao}^2 + \left(\frac{\delta\lambda}{rdisp}\right)^2} \qquad (16)$$

which gives the explicit relation of $\delta\phi_{graf,disp}$ and $rdisp$.

To get the insight into the tradeoff guiding the choice of the spectral dispersion value $rdisp$, let us introduce the dimensionless free width of FOV, Δw_{el}, expressed in the number of the spatial elements of resolution $\delta\phi_{graf,disp}$ as follows:

$$\Delta w_{el} = \frac{\Delta w_f}{\delta\phi_{graf,disp}} \simeq \frac{\frac{\Delta\lambda_f}{rdisp}}{\sqrt{\delta\phi_{ao}^2 + \left(\frac{\delta\lambda}{rdisp}\right)^2}} \qquad (17)$$

From the last equation and Eq.(8), it follows that when the spectral dispersion increases, i.e. $rdisp \to 0$, then:

$$\Delta w_{el} \to \Delta w_{el,max} = \frac{\Delta\lambda_f}{\delta\lambda} = \mathcal{F} \qquad (18)$$
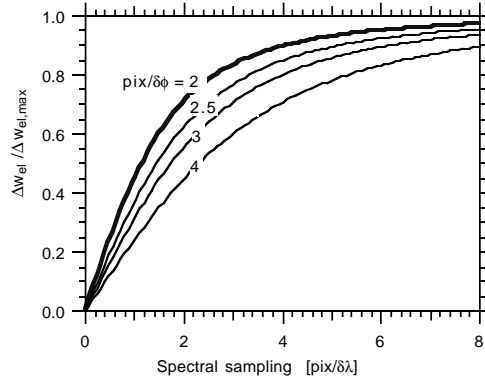
Figure 3. The ratio of the free width expressed in number of resolution elements Δw_{el} to its asymptotic maximum $\Delta w_{el,max} = \mathcal{F}$ in function of the spectral (along the grating dispersion) and spatial sampling ratios.

The finesse $\mathcal{F}$ sets the asymptotic upper limit to the number of spatial elements that one can get along the width of the GraF FOV. This is illustrated in Fig. 3, which displays the ratio of Δw_{el} to the possible maximum $\Delta w_{el,max}$ in function of the spectral sampling ratio along the grating dispersion ρ_λ. The latter is defined as the number of pixels for one element of resolution, $\rho_\lambda = \delta\lambda/rdsip$. The curves are computed for several values of the spatial sampling ratio, $\rho_s = \delta\phi_{ao}/H$.

One can see that $\Delta w_{el}/\Delta w_{el,max}$ increases rapidly up to $\rho_\lambda \simeq 2.5$ and saturates afterwards. The range of $rdisp$ and Δw_f corresponding to $\rho_\lambda \simeq 2.5$ can be considered as optimum. Higher dispersions will give only a slight increase of $\Delta w_{el}/\Delta w_{el,max}$, while the number of order windows covered by the detector, M_{wind}, will decrease linearly.

The numerical values of the free width Δw_f chosen for the instrument are close to the optimum. They and are given in Tab. III in *arcsec* and *pixels*. The corresponding value of Δw_{el}, for instance at $\lambda = 2.2$ μm, is $\Delta w_{el} \approx 7$. The other parameters are the platescale $H = 50$ mas/pix (hereafter mas states for $milli - arcseconds$), $rdisp$ of the 300 mm^{-1} grating, the free width $\Delta w_f = 1.55''$ and the measured psf extension $\delta\phi_{graf,disp} = 0.22''$ (see Sect. 10.1).

The maximum possible width at this wavelength is $\Delta w_{el,max} = \mathcal{F} \approx 16.8$, as calculated from $\Delta\lambda_f = 4.75$ nm and the measured spectral resolution $\delta\lambda = 0.3$ nm of the FPI. The measured ratio $\Delta w_{el}/\Delta w_{el,max} \approx 0.45$ is close to the theoretical value of 0.55 derived from Fig. 3 for the used spatial and spectral samplings ratios respectively $\rho_s = 2.6$ and $\rho_\lambda = 1.9$.

Ouput f/45 beam
to IR Camera

Space: 1.5 x 0.5 m, Weight 30 kg

10 cm

Field
Rotator

M_{out}

Grating

Focal aperture

M_{in}

Spectrograph camera

Collimator

Fabry-Perot
Interferometer

Input f/45 beam
from ADONIS
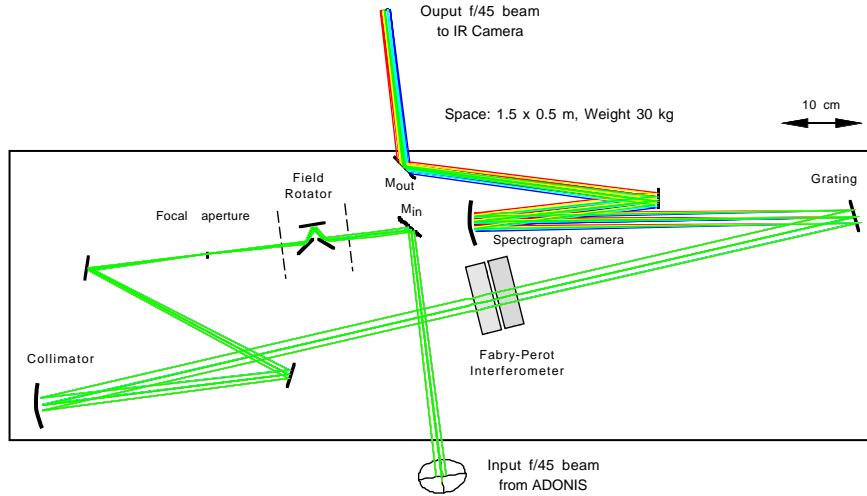
Figure 4. The GraF optical design.

7. Implementation at the telescope

7.1. Hardware

The implemented spectrograph has been designed to meet the ADONIS imposed mechanical constraints, dictating a compact (1.5 m × 0.5 m) and light (30 kg) instrument (see Fig. 4). The operating wavelength range from 1.2 μm to 2.5 μm corresponds to that of the SHARPII+ camera.

The spectrograph was installed at the ADONIS visitor equipment bench (Beuzit et al., 1997), located between the adaptive optics output and the SHARPII+ camera. The flat mirror M_{in} intercepts the ADONIS f/45 output beam and sends it into the spectrograph. The beam passes firstly through a field rotator made of a prism and a flat mirror. The field rotator of GraF allows to vary the slit orientation on the sky, which otherwise would have been remained fixed due to ADONIS constraints. The FOV is selected by the rectangular aperture located in the ADONIS focal plane. Its width, can be adjusted continuously and with a good precision from 0.1″ to 15″, and its height is fixed to about 30″. After the aperture, the beam is collimated, passes through the Fabry-Perot interferometer, is dispersed by the grating, reconfigured by the spectrograph camera back to the f/45 beam and sent to the SHARPII+ camera.

The instrument can also be used in a direct imaging mode, either by setting the grating at the zero order position, or replacing it by a

flat mirror mounted at the back of the grating (not shown in Fig. 4). In this configuration the FPI is used in the classical scanning mode.

The two flat mirrors M_{in} and M_{out}, located on the axis of the ADONIS-SHARPII+ camera, are mounted on a dedicated common support, so that they can be removed and installed within minutes, allowing a quick change from the GraF IFS mode to the regular ADONIS imaging observations.

The motors controlling the focal aperture, the field rotator, the grating position, the FPI in- and out- of the beam movements, are operated through the GraF dedicated version of the ADOCAM real-time operations software written by F. Lacombe. The GraF operation at the telescope thus inherited conveniently from the user-friendly interface of the wide-band imaging ADONIS observations, and in particular the possibility to launch the command sequences in the batch mode.

7.2. Optical quality

The necessity to fit the instrument into a reduced room implied adding 5 more flat mirrors in the optical design, further, the necessity of the field rotator implied adding 3 mirrors more. In total, it makes 11 reflecting surfaces. The loss in transmission is limited by the high efficiency golden coatings. However, this extra number of optical surfaces certainly decreased the spectrograph image quality. Estimating that a mirror is manufactured with $\lambda/10$ precision, and $\lambda = 0.6\ \mu m$, the accumulated rms wavefront error should be about $200\,nm$, or $\lambda/5$ at the shortest operating wavelength of $1.2\ \mu m$, which can be considered as still acceptable.

More importantly, these static aberrations, at least at low and moderate spatial frequencies, are corrected by the fine tuning of the AO, so that the degradation of the final image quality is negligible as witnessed by the stellar images given in Fig. 7. The AO tuning is done at the beginning of each night.

7.3. Observing modes

The Table I summarize the observing modes of the GraF instrument. It shows an apparently complex instrument, while in practice the change from one mode to another is done in a few dozen of seconds or in a few minutes at longest, and can be programmed beforehand using the ADONIS/ADOCAM control software scripts. The availability of the modes of direct imaging and of grating spectroscopy (hereafter GS) was very valuable during the tests, providing independent and complementary measurements for the IFS mode. Furthermore, the GS mode

Table I. The summary of the available observing modes.

Mode	Focal aperture	FPI	Grating position
Direct Imaging	Open J & H: $9'' \times 9''$ K: $12.8'' \times 12.8''$	Out	Zero order, or Flat mirror
Grating spectros.	Open, or narrow slit J & H: $\simeq 0.2'' \times 9''$ K: $\simeq 0.2'' \times 12.8''$	Out	chosen λ
Scanning IFS	Rectangular J & H: $\simeq 0.8'' \times 9''$ K: $\simeq 1.5'' \times 12.8''$	In	chosen λ, compensation of the λ-shift induced by the FPI scan
Scanning FPI imaging spectroscopy	Open J & H: $9'' \times 9''$ K: $12.8'' \times 12.8''$	In	Flat mirror

was extensively used for observations of "linear" objects like binary stars.

The grating is mounted on a high quality turning support, so that the grating angle settings are of a high precision insuring an accurate and stable wavelength setting. This was of special importance for the IFS mode. Indeed, during the FPI scanning the image on the detector undergoes slight shifts along the λ-axis. We used an automatic procedure compensating these shifts by changing the grating angle at each change of channel in order to keep the image as precise as possible at the same detector pixels and thus to decrease the uncertainties of the flux estimate.

7.4. Optical parameters

The spectral resolutions are listed in Tab. II. The Table III gives the main parameters of the GraF IFS mode: the reciprocal dispersion $rdisp$, the free FOV width Δw_{pix} and Δw_{arc}, and the number of order windows covered by the detector, M_{ord}. The parameters are listed for the 2 gratings available in the IFS mode and for the mostly used platescale $H = 50$ mas/pix. The parameters for two other available platescales, 35 mas/pix and 100 mas/pix, can be obtained by applying the scaling factor, except Δw_{arc} which does not depend on H.

The FPI, fabricated by Queensgate Inc. according to our specifications, has the following parameters: the interorder spectral spacing

Table II. Spectral resolving power. For the grating spectroscopic mode, it corresponds to the slit width of 0.2''.

$\lambda(\mu$m)	IFS and FPI modes	Grating Spectroscopy		
		35 mm^{-1}	300 mm^{-1}	600 mm^{-1}
1.25	16000	200	1200	2500
1.65	10000	300	1600	3500
2.2	7000	600	4000	10000

10.1096±0.0005 cm^{-1}, the finesse $\mathcal{F}$ about 20 depending on the wavelength, the optical transmission in peaks about 85%. The FPI has two operating spectral ranges, $\lambda\lambda$ $1.2 - 2.5$ μm and $\lambda\lambda$ $3.8 - 4.5$ μm, due to the plates coating proposed by E. le Coarer. Only the first range was used with the GraF/ADONIS instrument.

7.5. THERMAL BACKGROUND

The thermal background of a non-cooled spectrograph is significant at $\lambda > 2$ μm. It was the subject of a special analysis during the design phase. Let us remind that the main source of the thermal emission is the warm environment of the grating. Indeed, contrary to a mirror with the bi-univocal correspondence between the incoming and reflected beams, a grating has more than one order of interference and consequently more than one input lobes corresponding to the output beam. It is a well known problem in the visible spectroscopy solved by limiting the detector passband by an order blocking filter. To reduce the thermal background, we adopted a similar solution, so that as a rule the spectroscopy at $\lambda\lambda$ $2 - 2.5$ μm was done using the cooled circular variable filter (CVF) (see Hofmann et al., 1995). Its passband $\lambda/\Delta\lambda \simeq 50$ fitted nicely the spectral range covered by the NICMOS detector with the 300 mm^{-1} grating the most frequently used in the IFS mode.

7.6. MEASURED SENSITIVITY

The measured limiting magnitudes m_{lim} in the two main spectroscopic modes are listed in Table IV. In the J and H bands, m_{lim} is very close to the values derived from the limiting magnitudes of the broad-band imaging (Le Mignant et al., 1999) and the theoretical GraF throughput of 0.64 for the GS mode and of 0.54 for the IFS mode. The throughput was calculated taking the reflexion coefficient of 7 mirrors equal to 0.98 each, the transmission of the FPI of 0.85, the efficiency of the grating of

Table III. Parameters of the IFS order window for the platescale 50 mas/pix. The
FPI interorder spectral spacing $\Delta\sigma_f = 10.1096\ cm^{-1}$.

λ	Grating 300 mm^{-1}				Grating 600 mm^{-1}			
	Disp.	Free FOV width		M_{ord}	Disp.	Free FOV width		M_{ord}
μm	nm/pix	arcsec	pix		nm/pix	arcsec	pix	
1.2	0.1655	0.43	8.70	29	0.0767	0.94	18.8	13
1.6	0.1621	0.79	15.8	16	0.0707	1.81	36.2	7
2.2	0.1558	1.55	31.1	8	0.0581	4.17	83.3	3
2.5	0.1520	2.06	41.1	6	0.0494	6.32	126.5	2

Table IV. The measured limiting magnitudes for
S/N=5 with the grating 300 mm^{-1}. The integration
time for the IFS mode is given per frame. For the
grating spectroscopy, the values are given for the slit
width of 0.2″. The spectral resolutions are those of
Table II.

Mode	Exp. time (min.)	J	H	K
IFS	1	8.5	9.4	9.3
	5	10.4	11.1	10.0
Grating	5	10.6	11.4	10.6
Spec.	30	12.1	12.9	11.5

0.80, and the transmission of the field rotator of 0.94. In the K band,
for the exposures shorter than 1 min in the GS mode and 5 min in
the IFS mode, the noise is dominated by the detector read-out noise
($\simeq 35$ electrons); above this time, the noise is dominated by that of the
thermal background.

8. Observing procedures and calibrations

We will limit the discussion of the observing procedures to the IFS mode
and to particularities of the GS mode, other modes being classical.
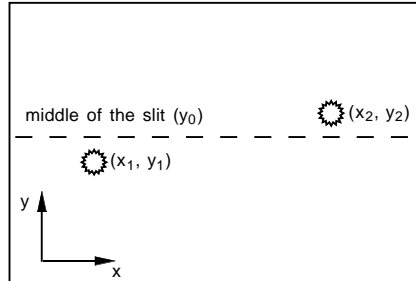
Figure 5. The entrance field of view in the slitless GS-spectroscopic mode operation. A direct imaging exposure giving the y-positions of the stars relative to the middle of the slit allows to adjust the zero's of the wavelength scales of the stellar spectra.

8.1. Grating long slit and slitless spectroscopy

The sharpness of the AO psf $\mathcal{P}$ with $\delta\phi \simeq 0.1'' - 0.2''$, much steeper than that of seeing limited observations (e.g. Racine, 1996), is a new element to take into account for the GS observations. Setting the slit width close to the extension of $\mathcal{P}$ as it is usually done for seeing limited observations, can give rise instrumental effects which could be neglected so far, like e.g. diffraction at the slit border. With the rapidly variable psf $\mathcal{P}$, these effects are difficult to calibrate. Also, the acquisition of the star on the center of the slit of only $\approx 0.1''$ - $0.2''$ wide can take considerable telescope time.

To avoid these losses, we let whenever possible the entrance aperture wide open (several arcsec), the sharpness of $\mathcal{P}$ already insuring a well defined spectrum. The important caution in this slitless mode of observations was to take a direct image of the field to record the accurate positions of the star(s) producing the spectrum (see Fig. 5). The difference of the stellar y-positions relative to the middle of the slit provides then the value of the translation to be applied to the wavelength calibration obtained as usually on a calibration spectral lamp with a narrow slit.

8.2. Calibrations

The main instrumental effects implying the calibration exposures were the usual detector pixel-to-pixel response and bias values, and the spectral setting parameters. The complete set of GS data of an object is as follows (with the typical global telescope time given in parenthesis):

−   Scientific long slit or slitless GS frame (10-30 min);

- Image frame of the spectroscopic field of view; Particularly important for slitless GS to define the translation of the wavelength calibration (1 min);

- Long slit spectrum of the "flat-field" produced by a tungsten lamp illuminating the entrance ADONIS pupil; gives the calibration of the detector pixel-to-pixel variations of sensitivity; the slit width $0.2''$ - $0.4''$ (needs the interruption of the AO servo-loop, 5 min);

- Long slit spectrum of a spectral Ar or Ne lamp, providing the wavelength calibration; the slit width $0.2''$ (1 min, done during the same interruption of the AO servo-loop as the "flat-field" spectrum);

While the wavelength calibration was reliable and better than 0.01% (see Sect. 10.1), the "flat-field" calibration of the pixel-to-pixel variations of sensitivity turned out to be troublesome. It turned out that the design of the SHARPII+ camera optics and that of the NICMOS detector conspired in the way to modulate the overall spectral response by the interference fringes formed by the sapphire substrate of the detector (see Fig. 6). At some wavelengths, the amplitude of the fringes was up to 20% peak-to-peak. More importantly, the fringe pattern could vary, by translation due to probably mechanical flexure, and also due to variations of the NICMOS pixels sensitivity. It was therefore mandatory to take the "flat-field" spectra very close in telescope position and time to the object spectrum. With all cares taken, the residual fringing was still about 1%, and sometimes worth.

A typical IFS data set is as follows:

- The IFS cube of data on the object (from 20 min for exposures of 15 s per frame up to about 1 hour for 60 s per frame);

- Direct image of the field of view (1 min);

- IFS "flat-field" cube (5 - 10 min);

- IFS spectral lamp cube, with the FPI scanning limited to about 10 steps around a prominent spectral line of Ar or Ne, providing the IFS cube wavelength calibration and the measurement of the FPI spectral response (5 min).

The parallelism of the FPI plates is checked and adjusted in the beginning of each night.
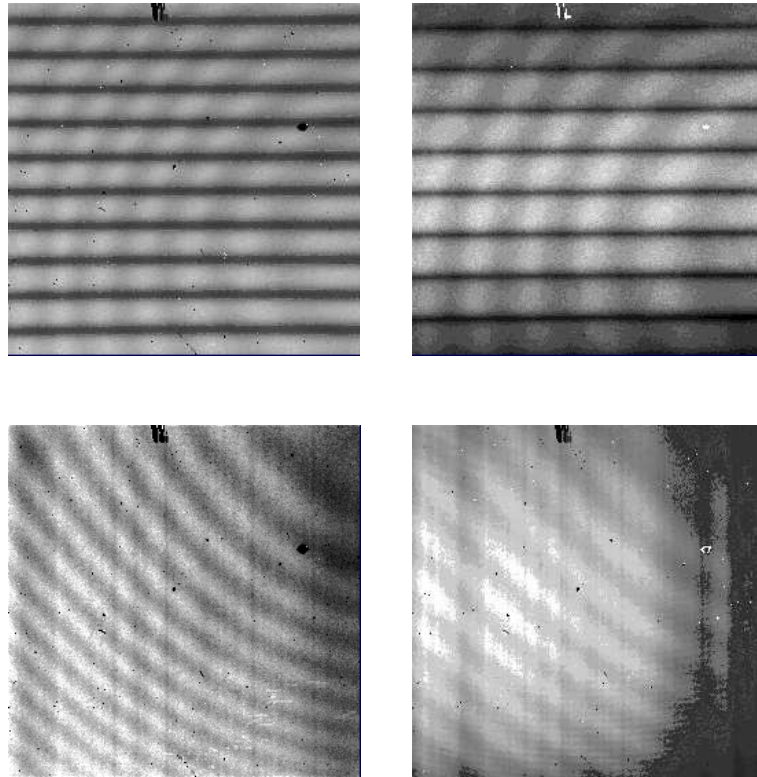
Figure 6. Flat-field frames in the 3D-mode (top) and in the long slit mode (bottom), at $\lambda = 1.6 \ \mu m$ (left), and at $\lambda = 2.2 \ \mu m$ (right).

9. Data reduction

Although the deconvolution is an integral part of the spectrum extraction in the case of scarcely resolved objects (see Sect. 2), a complete discussion of the possible strategies in different types of situations is largely out of the scope of the present paper. Here, we will describe only the procedures used to extract the spectra of the complex central region of η Car object chosen to test the instrument performances at the limit of the resolution.

9.1. Preliminary steps

They were as follows:

−   The frame "cleaning" for irrelevant pixel values. It was done using a median filter with the adaptive threshold and the area size, which can run along columns, lines, or square areas according to best

final result. The irrelevant pixel values were replaced by the 2-dimensional linear interpolation.

— Dark frames subtraction;

— Flat-field division.

9.2. Spectrum extraction. GS mode

Since at the beginning of every run the detector was aligned so that its lines were parallel to the the slit. The grating dispersion is then parallel to the detector columns at least in first approximation. However, the parabolic aberration usual to grating spectrographs makes a stellar spectrum to be a slightly curved line. We therefore extracted the spectra of stellar sources by fitting the psf $\mathcal{P}$ line by line, with the multiplicative factor A (amplitude) and the position across the dispersion as the fit parameters. The amplitude A gives the estimate $\hat{S}$ of the flux density. The psf $\mathcal{P}$ is the average of several lines selected in the continuum of an isolated star, if possible the studied object, otherwise a reference star off the field.

If the spectrum was obtained as a slitless (see Sect. 8.1), the calibration of the line number *vs* the wavelength λ is done taken into account the position of the star with respect to the slit center.

The spectrum of a standard star in Fig. 9 (dotted line) gives an example of the final result.

9.3. Spectrum extraction. IFS mode

9.3.1. *Isolated stars*
The spectrum extraction for an isolated star is done by fitting a two-dimensional normalized psf $\mathcal{P}$ to each order image of a channel frame with the amplitude A and the $\{x, y\}$ position as the fit parameters. As in the GS case, the amplitude A is used as the estimate $\hat{S}$ of the flux density F, and after the wavelength calibration the vector $\hat{S}$ *vs* λ provides then the stellar spectrum (Fig. 9, solid line).

The psf $\mathcal{P}$, constructed as the "shift-and-add" average of the images corresponding to the stellar continuum, is normalized so that the integral of the signal over the psf area is equal to one. This normalization makes the fit amplitude insensitive to the variations of the Strehl ratio from one channel frame to another.

If each channel frame contains orders corresponding to the stellar continuum, then one can monitor the channel-to-channel photometric variations. Obviously, the continuum orders must be selected as free

as possible from the telluric absorptions. The channel-to-channel variations of the average flux are assumed then to be photometric and give the correction factor. The method was successfully tested on the data of HR8353 (see Sect. 10.1).

9.3.2. *Complex objects with the features at the psf scale*

The deconvolution becomes then unavoidable. Comparison of different strategies being out of the scope of the present article, we can give only a short description of the recipes used during the data reduction of the test case of the η Car central region (see Sect. 10.2

Firstly, the psf $\mathcal{P}$ is constructed as described for the isolated stars cases. Then the Richardson-Lucy (RL) deconvolution algorithm was run on the cube frames. The RL algorithm provides a sharpened image clarifying the structure of the object. However, the resulting flux distribution is unreliable for the quantitative analysis (e.g. Magain et al., 1998), and must be found by other methods.

So that at the next step we used a simple physical modeling of the studied region best fitting the data. Thus the model for η Car consisted of point sources at the positions found by RL algorithm.

The distance between the secondary spots in *eta* Car, down to 0.11arcsec, being too close to the resolution limit (0.11arcsec at λ $1.7\mu m$), the uncertainties of the model fitting turned out to be too important to be used for the spectrum extraction.

We used then a specific to η Car additional information provided by the photocenter spectral dependence in the way known as the differential "super-resolution" (Beckers, 1982, Tokovinin, 1992). This allowed us to separated the spectrum of the bright star and the remaining secondary objects (see for details Sect. 10.2).

9.3.3. *Software*

We used the Khoros 2.1 software integration and development environment, which provides the visual programming of data flows and an extended library of routines suitable for the reduction and analysis of data up to 5 dimensions (KRI, 1996). When necessary, GraF specific routines were developed and added to the Khoros library .

10. Example and quality of the IFS data

We present and discuss below the instrument performances in terms of spectroscopic and imaging capabilities measured in two relevant test cases.

The first case is a single standard star. Its measurement provides a reliable estimate of the quality of the spectrum extracted from the IFS data. We show in particular that recording the stellar light simultaneously in several spectral "windows" allows to accurately monitor the channel-to-channel variations of flux count estimates.

The second case is the observation of the central $0.9'' \times 0.9''$ region of η Car, well studied by previous research groups. It provides an excellent test of spectro-imaging ability of the instrument in a complex field with the spatial structure at scales down to the limit of the angular resolution (about $0.1''$) as well as the spectral line profile structure at scales close to the limit of the GraF spectral resolution (about $10\,000$ in this case).

10.1. Spectrum of a standard star

A IFS set of data on a standard star HR8353 B3III, K = 3.31 mag (van der Bliek et al., 1996) was obtained in November 1997. The spectral range covering about 40 nm was centered on the hydrogen Br-γ 2165.55 nm line. The FPI interorder spectral spacing of about 4.75 nm was covered by 48 FPI channel frames with the spectral step between the channels of $9.895 \cdot 10^{-2}$ nm as measured in the FPI order m = 457. We used the SHARPII+ platescale of 50 mas/pix and the grating of 300 mm^{-1} (see Tab. III for other parameters). One channel frame records here 8 FPI order images, the total number of spectral points is thus $48 \times 8 = 384$. The exposure time per channel was $10\,\mathrm{s}$.

A strip with the stellar images recorded in the first channel is reproduced in Fig. 7 (left). The good image quality of GraF data is witnessed by the sharpness of the flux distribution with FWHM $\simeq 0.13''$ across the grating spectral dispersion, as one would expect for the diffraction limited image. Along the dispersion, FWHM $\simeq 0.22''$, as one expects for the convolution product of the diffraction limited image with the spectral response of the FPI and the grating (see Sect. 6.2 and Eq.(16)).

The data reduction steps after the usual bias subtraction and correction for the pixel-to-pixel variations were as follows. Firstly, the psf $\mathcal{P}$ was estimated separately for each channel as the "shift-and-add" average of the stellar images in the continuum. Then the flux count in each order window was estimated by fitting $\mathcal{P}$ to the stellar images, with the flux count and the image photocenter as the free parameters. The flux estimate in function of the spectral point number is plotted in Fig. 8 (top). The spectral point numbers are in the order of increasing λ. One can see strong variations of the flux estimate correlated with the channel number.

We selected the order windows free of stellar and telluric spectral lines, and imposed the condition such that the total stellar flux in those
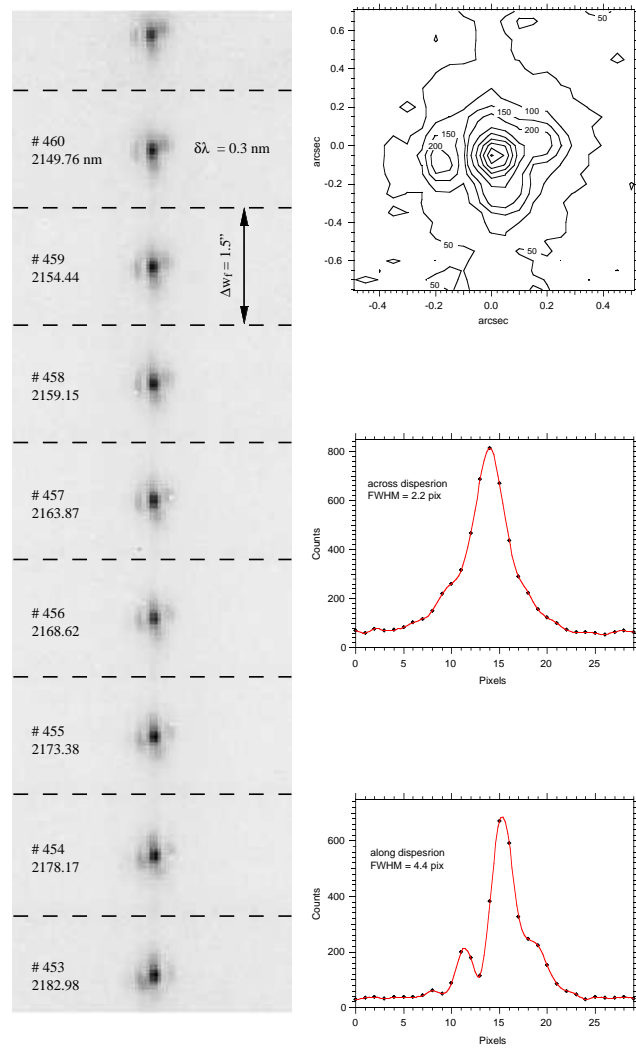
Figure 7. A channel frame of the IFS cube of the standard star HR5383.
Left panel: The central strip of the frame corrected for the detector bias and pixel-to-pixel sensitivity variations. The dashed lines indicate the spatial limits of the FPI order windows. The spectral passband of window $\delta\lambda = 0.3$ nm, or R $\simeq 7000$.
Right panel: The point-spread function extracted from the order 459. *Top:* The contour map of the stellar image. The contour decrement is 100 counts above the 200 counts level. *Middle and bottom*: The counts distribution through the maximum respectively across and along the spectral dispersion; the FWHM $\delta\phi_x = 2.6$ pix $(0.13'')$, and $\delta\phi_{graf,disp} = 4.4$ pix $(0.22'')$.

windows is the same for all channels, which is the definition of the stellar continuum. The channel-to-channel variations of the so defined
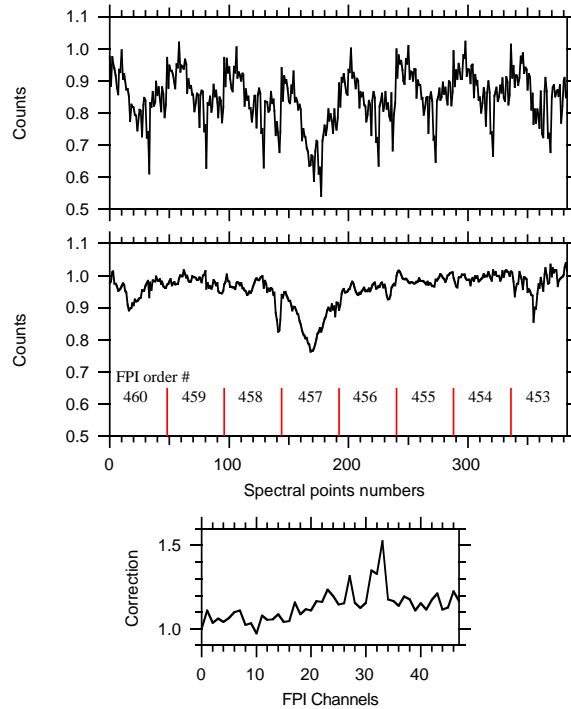
Figure 8. Correction for the "photometric" variations during the FPI scan.
Top and middle: Flux counts estimate in the channels before (top) and after (middle)
the correction for counts variations. The FPI order numbers and their spectral limits
are indicated in the middle plot. The scan consists of 48 channels. One channel covers
8 FPI orders, the scan results in 384 spectral points. The points are numbered in the
order of the increasing wavelength. *Bottom:* The photometric correction vs channel.
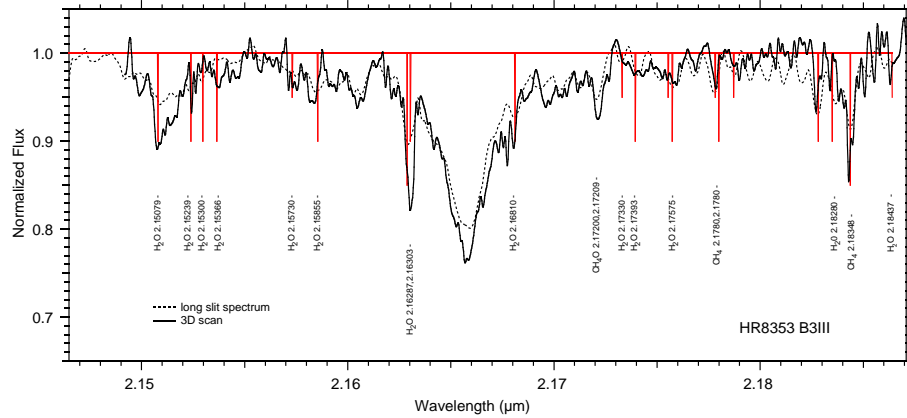
Figure 9. Spectrum of a standard star HR8353 extracted from the IFS cube, cor-
rected for the channel-to-channel counts variations and calibrated in wavelength.
The spectrum obtained in the long slit mode is also plotted as the dashed line. The
identified telluric lines are indicated by vertical bars.

total flux are then ascribed to the photometric variations, and used to calculate the correction factor plotted in Fig. 8 (bottom). Applying the correction factor to the extracted spectrum resulted in the rectified spectrum shown in Fig. 8 (middle) and Fig. 9.

In fact, the described channel-to-channel variations were mostly due to the method used for the flux estimate, the psf $\mathcal{P}$ fitting, which is sensitive to the Strehl ratio, varying with time. Using other methods, e.g. integrating on the area of the stellar image gives much better results. However, we took profit of this data reduction misadventure to demonstrate the possibility of accurate correction of photometric variations.

The wavelength calibration accuracy was estimated by measuring the agreement between the expected and the measured positions of the telluric lines. It was excellent with the relative rms error in λ being $4 \cdot 10^{-5}$.

The S/N ratio estimate is biased by the numerous at this sensitivity faint ($\leq 1\%$ of the continuum) telluric absorptions due to $H_2 0$, CH_4, etc., mostly identified in Fig. 9, using the tables by Mohler (1955). The lower limit S/N > 100 (1 standard deviation) was measured on 50 points of on the less contaminated spectral interval starting from $\lambda 21800$ nm. An additional estimate was obtained from the GS data recorded as a sequence of 10 identical exposures. The variations of the flux counts from one exposure to another gave the estimate S/N$\simeq$ 300, close to the expected from the photon statistics for this bright star.

10.2. IMAGING SPECTROSCOPY OF MULTIPLE SPOTS IN THE η CAR CENTRAL REGION

The η Car object is a luminous star loosing mass in giant eruptions (see review by Davidson and Humphreys, 1997). The central region contains several point-like sources as illustrated in Fig. 10, the bright spot A of η Car, and the B, C and D spots at the distance $0.1'' - 0.3''$ to the NW from the central star (Weigelt and Ebersberger, 1986). Davidson et al. (1997), using HST/GHRS, obtained the UV-spectroscopy of the B, C and D spots, showing them to be dense, compact slow-moving ejecta emitting in narrow forbidden emission lines of FeII. The stellar core emits in broad permitted emission lines formed in the dense fast stellar wind (see also Hamann et al., 1994 for the ground-based spectroscopy of η Car with the angular resolution $\delta\phi \approx 5''$ and the spectral resolution R $\approx$ 3000 in the near IR, and Hillier et al., 2001 for the HST/STIS spectrum of η Car spot A in the the 164 - 1040 nm spectra range with $\delta\phi \approx 0.25''$ and R up to 5000).
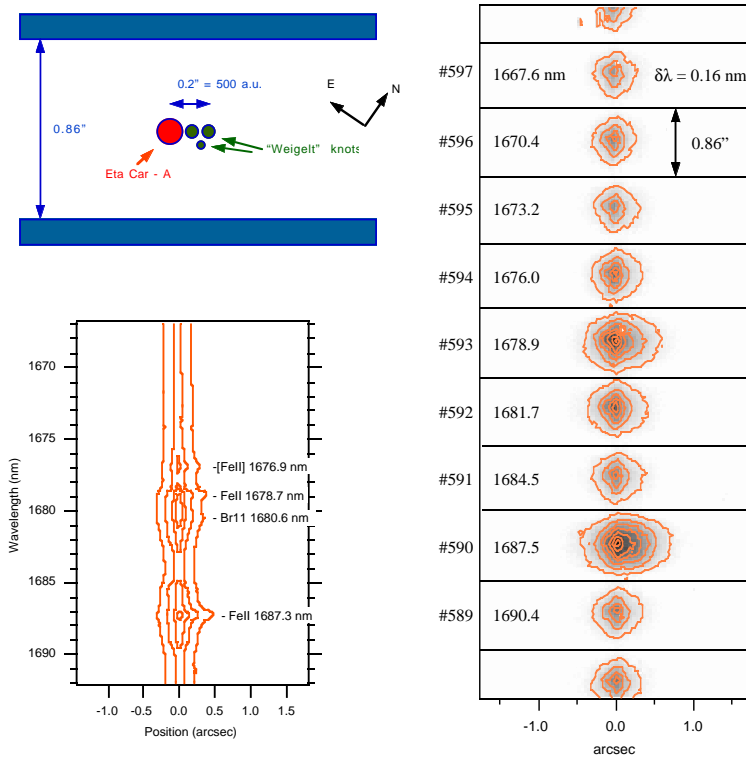
Figure 10. Imaging spectroscopy of η Car in the 1668-1692 nm range. *Left top:* The FOV of the IFS cube. *Left bottom:* The long slit spectrum; the slit width $0.2''$, spectral resolution $\simeq 3500$. The contours are at 500, 1500, 2500, 3500 and 4500 counts. *Right* The channel frame 44 of the η Car IFS cube. The FOV and the spectral settings are indicated; spectral resolution $\simeq 10000$.

10.2.1. *Observations*

The observations of η Car were done on Nov. 15, 1997 at UT 9:00-9:20. We selected the spectral range 1668-1692 nm, since it fortunately includes several spectral transitions of various excitation, namely the hydrogen Br11 1680.6 nm, [FeII] 1676.9 nm, FeII 1678.7 nm, and FeII 1687.3 nm (Hamann et al., 1994). The overview of the spectrum is given by the long slit spectroscopy frame (Fig. 10) taken with the slit centered on the spot A and turned to the positional angle PA=311°, between those of the B and C spots at PA=340° and PA=296.5° respectively (Hofmann and Weigelt, 1988). The exposure time was 15 s, and the spectral resolution $R \simeq 3500$.

The IFS data were taken with the platescale 35 mas/pix and the grating 300 mm^{-1}. The FOV width was $0.86''$, and the height $9.0''$. The height is fixed by the detector format. The positional angle of the IFS observations was the same as for the GS data, PA=311°. The cube

consisted of 48 channel frames of the FPI. Each channel frame records the FOV in 9 order windows with the passband $\delta\lambda = 0.16$ nm each, or R = 10 000. The exposure time per channel was 5 s.

The instrumental performances in terms of the image quality and deconvolution can be illustrated and discussed on the example of one channel frame. The full set of data will be presented and discussed elsewhere together with its astrophysical implications.

10.2.2. *Deconvolution*

Already the visual inspection of the cube shows that at the wavelengths of [FeII] 1676.9 nm, FeII 1678.7 nm and 1687.3 nm lines the η Car image is extended. For the following discussion we selected the channel frame 44, where the emission in these lines is at maximum (see Fig. 10, orders 593 and 590, corresponding respectively to FeII 1678.7 nm and 1687.3 nm). On the other hand, the η Car image in the continuum emission, orders 595-597, is that of a point-like source, so that we could select one of the orders, namely 596, as the psf $\mathcal{P}$ for the deconvolution.

The frame was deconvolved using the Richardson-Lucy maximum likelihood algorithm (Lucy, 1974, Hook and Lucy, 1994), stopped after 50, 200 and 1000 iterations. The results obtained with 200 iterations were selected as the best compromise between the attained resolution and the level of artifacts. They are displayed in Fig. 11. The regular and sharp appearance of the stellar image in the order 591, produced by solely continuum emission and therefore corresponding to the unresolved stellar core, witnesses the good quality of the deconvolution and absence of artifacts. The FWHM of this image is $0.1''$, very close to the diffraction limit of the telescope.

In contrast, the image in the FeII line order 590 shows a complex structure. The flux profile across the dispersion (Fig. 11, bottom) has two secondary maxima, at $0.13''$ and $0.24''$ from the primary. This is in a good agreement with the values of $0.114''$ and $0.211''$ given for B and C spots by Hofmann and Weigelt (1988), indicating thus the good quality of the deconvolved GraF data. The D spot is not seen probably due to its faintness.

10.2.3. *Spatially resolved spectra*

To complete the task of the imaging spectroscopy as it was discussed in Sect. 2, we have to solve the image restoration problem and find the set of estimates $\hat{S}(x, y, \lambda)$ of the flux density distribution.

Unfortunately, the Richardson-Lucy deconvolution does not restore properly the flux distribution, enhancing artificially the sharp sources.

We therefore tried the model fit method. The flux distribution estimate $\hat{S}$ was modeled as as set of monochromatic functions $\hat{S}_\lambda(x, y)$
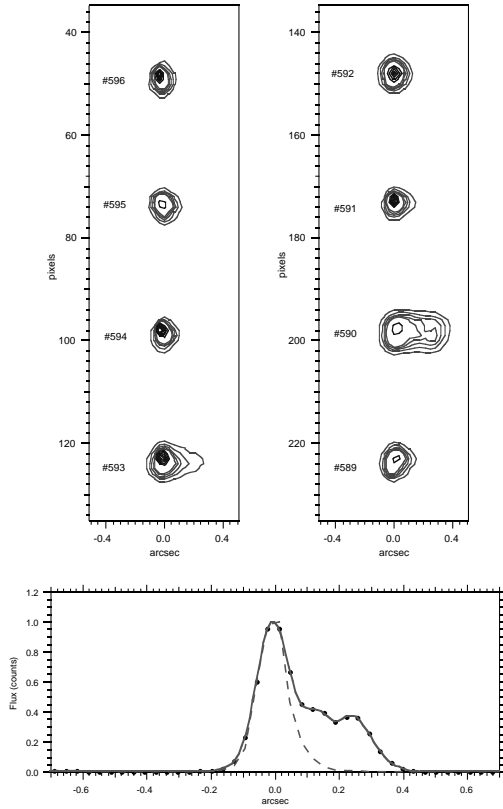
Figure 11. Top: The deconvolved η Car image in the channel frame 44. *Bottom:* The flux profiles across the spectral dispersion in the orders 590 (solid line) and 589 (dashed line). The profiles are normalized to the maximum value. The secondary maxima in the order 590 are at $0.13''$ and $0.24''$ from the maximum flux.

consisting of a primary point-like object surrounded by 1, 2 or 3 secondary point-like objects. The model function is then convolved with $\mathcal{P}$ and we look for $\hat{S}$ giving the best fit to the observed flux distribution $F_\lambda(x, y)$. However, no fit gave satisfaction, either showing too high residuals (models with 1 and 2 secondaries), or a too shallow likelihood maximum (models of 3 secondaries) implying highly uncertain fluxes and positions.

This is not very surprising given that the separation of the A, B and C spots is very close to the angular resolution limit of the telescope $\delta\phi \simeq 0.1''$ at this wavelength.

The way turned to be fruitful was taking into account the additional information provided by the photocenter spectral dependence, following the ideas of the differential "super-resolution" approach (Beckers, 1982, Tokovinin, 1992). The Fig. 12 displays the integrated spectrum of the

whole $0.9'' \times 0.9''$ region in the FeII 1687.3 nm line (top), and the photo-
center (center of gravity) position across the dispersion *vs* wavelength
(bottom). The photocenter remains constant all along the continuum
emission and along the broad wings of the FeII line. It deviates up
to 150 mas in strong correlation with the narrow spectral emission
appearing at the top of the broad spectral line.

The spectra are separated if we assume a simple model where η
Car is composed of 2 objects: the unresolved bright primary (spot A)
and an "ejecta cloud", which includes both the B and C spots and,
possibly, a halo. Indeed, then the photocenter drift indicates that the
the broad emission comes from the spot A, while the narrow emission
well correlated with the deviation of the photocenter comes from the
"ejecta cloud".
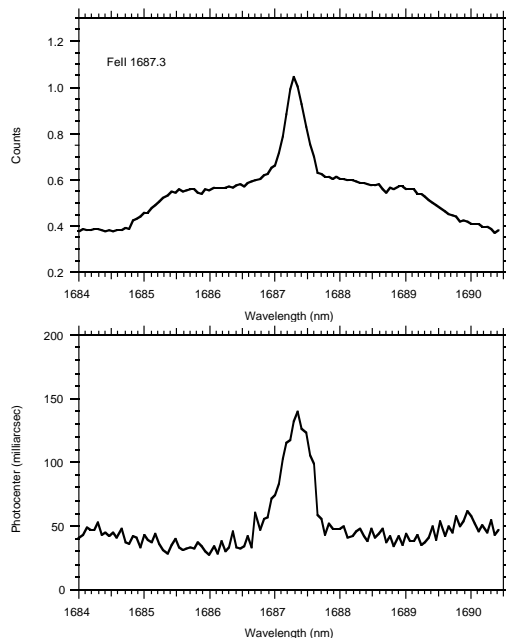
Figure 12. Top: The profile of FeII 1687.3 nm in the spectrum of η Car. *Bottom:*
The corresponding drift of the photocenter *vs* wavelength.

One can derive the parameters of the "cloud" emission as follows:
$\text{FWHM} \simeq 80\,\text{km} \cdot \text{s}^{-1}$ and $\text{FWZM} \simeq 180\,\text{km} \cdot \text{s}^{-1}$. The broad emission of
the primary spot A has $\text{FWZM} \simeq 900\,\text{km} \cdot \text{s}^{-1}$. The ratio of the total flux
emitted in the line by the "cloud" to that of the primary is about 0.4.
The "cloud" emission in the FeII 1678.6 nm line has similar properties.

The presence of emission of two kinds in the near IR lines, one with
a large velocity dispersion, coming from the stellar wind, and another

with a low velocity dispersion, has been already reported by Hamann et al. (1994), who suggested that the first one may arise in a disk surrounding the star. The GraF data obtained at a higher spectral and spatial resolutions showed for the first time the velocity resolved profile of the narrow FeII 1676.9 nm emission and clearly indicate that it arises in the ejecta composed of B and C spots to the NW from the bright primary A, in a good qualitative agreement with the work of Davidson et al. (1997).

Clearly, more information can be extracted from the present data, using additional spectral lines, etc. This will be presented in a forth-coming article, the discussion of this section being a mere illustration of the instrument performances.

11.   Conclusions and prospects

The GraF instrument for imaging spectroscopy based on the Fabry-Perot interferometer in the cross-dispersion with a grating was successfully tested and operated at the 3.6 m telescope with the ADONIS adaptive optics, allowing to combine the spectral resolution up to 10 000 with the high angular resolution of $0.1''$ - $0.2''$ provided by ADONIS. The ability of simultaneous imaging in several spectral passbands proved to allow in certain cases the simultaneous calibration of the spatial point-spread function $\mathcal{P}$. The subsequent deconvolution of data in the crowded field of η Car is shown to be of a high quality, with the final angular resolution close to $0.1''$ at $\lambda = 1.7$ μm, close to the telescope diffraction limit, in spite of the fact that at this rather short wavelength the adaptive optics correction of the atmosphere induced wavefront perturbations was only partial, and the point-spread function was highly variable in time.

The simultaneous mapping of η Car with resolutions R up to 10 000 and $\delta\phi \approx 0.1''$ achieved from the ground with ADONIS/GraF in the 1.7 μm spectral range compares favorably with R up to 5 000 and $\delta\phi \approx 0.1''$ obtained on the same object with the space-born instrument HST/STIS in the visible and far-red spectral range (Hillier et al., 2001).

In its practical aspects, the optical concept of the FPI cross-dispersed with a grating proved to be compact and versatile, allowing to switch to the long-slit spectroscopy, or to direct imaging within a minute.

The potential of the GraF concept has been further proven by the construction of new instruments either adopting its principles as the GriF scanning integral-field spectrograph for the CFHT (Clénet et al., 2000, Clénet et al., 2002), or developing them further as the Tunable Echelle Imager (Baldry and Bland-Hawthorn, 2000).

High quality data were obtained during the period of the scientific use of the instrument at the telescope in 1998-2001 on different programmes of stellar physics. They will be a subject of forthcoming papers.

References

Bacon, R., G. Adam, A. Baranne, G. Courtes, D. Dubet, J. P. Dubois, E. Emsellem, P. Ferruit, Y. Georgelin, G. Monnet, E. Pecontal, A. Rousset, and F. Say: 1995. *Astron. Astrophys. Suppl. Ser.* **113**, 347.

Baldry, I. and J. Bland-Hawthorn: 2000. *PASP* **112**, 1112.

Beckers, J.: 1982. *Opt. Acta* **29**, 361.

Beuzit, J.-L., L. Demailly, E. Gendron, P. Gigan, F. Lacombe, D. Rouan, N. Hubin, D. Bonaccini, E. Prieto, F. Chazallet, D. Rabaud, P.-Y. Madec, G. Rousset, R. Hofmann, and F. Eisenhauer: 1997. *Experimental Astronomy* **7**, 285.

Bland-Hawthorn, J.: 1995. In: *ASP Conf. Ser. 71, Tridimensional Optical Spectroscopic Methods in Astrophysics, G. Compte and M. Marcelin; Eds.* p. 369.

Chabal, R. and R. Pelletier: 1965. *Jap. J. Appl. Phys. Suppl. I* **4**.

Chalabaev, A., E. le Coarer, and D. Le Mignant: 1999a. In: *ASP Conf. Ser. 188: Optical and Infrared Spectroscopy of Circumstellar Matter.* p. 315.

Chalabaev, A., E. le Coarer, P. Rabou, Y. Mignart, P. Petmetsakis, and D. Le Mignant: 1999b. In: *Astronomy with adaptive optics: present results and future programs, D. Bonaccini, ed., ESO Conference and Workshop Proceedings*, Vol. 56. p. 61.

Chalabaev, A., D. Le Mignant, and E. le Coarer: 1999c. In: *Astronomy with adaptive optics: present results and future programs, D. Bonaccini, ed., ESO Conference and Workshop Proceedings*, Vol. 56. p. 491.

Clénet, Y., R. Arsenault, J. Beuzit, A. Chalabaev, C. Delage, G. Joncas, F. Lacombe, O. Lai, E. LeCoarer, D. Le Mignant, S. Pau, P. Rabou, and D. Rouan: 2000. In: *Adaptive Optical Systems Technology, Peter L. Wizinowich ed., Proc. SPIE*, Vol. 4007. p. 942.

Clénet, Y., E. Le Coarer, G. Joncas, J.-L. Beuzit, D. Rouan, A. Chalabaev, P. Rabou, R. Arsenault, C. Delage, C. Marlot, P. Vallée, B. Grundseth, J. Thomas, T. Forveille, O. Lai, and F. Lacombe: 2002. *PASP* **114**, 563–576.

Close, L. M.: 2000. In: *Adaptive Optical Systems Technology, Peter L. Wizinowich ed., Proc. SPIE*, Vol. 4007. p. 758.

Connes, P.: 1970. *Ann. Rev. Astron. Astrophys.* **8**, 209.

Cornwell, T. J.: 1992. In: *ASP Conf. Ser. 25: Astronomical Data Analysis Software and Systems I.* pp. 163–+.

Courtes, G.: 1982. In: *ASSL Vol. 92: IAU Colloq. 67: Instrumentation for Astronomy with Large Optical Telescopes.* p. 123.

Cox, P., P. J. Huggins, J.-P. Maillard, E. Habart, C. Morisset, R. Bachiller, and T. Forveille: 2002. *Astron. Astrophys.* **384**, 603.

Davidson, K., D. Ebbets, S. Johansson, J. A. Morse, and F. W. Hamann: 1997. *Astron. J.* **113**, 335.

Davidson, K. and R. M. Humphreys: 1997. *Ann. Rev. Astron. Astrophys.* **35**, 1.

Eisenhauer, F., M. Tecza, S. Mengel, N. A. Thatte, C. Roehrle, K. Bickert, and J. Schreiber: 2000. In: *Proc. SPIE Vol. 4008, Optical and IR Telescope Instrumentation and Detectors, M. Iye; A. F. Moorwood; Eds.* p. 289.

Fabry, C.: 1905. *C.R. Acad. Sci. Paris* **140**, 848.

Goodman, J.: 1968, *Introduction to Fourier Optics.* McGrow - Hill.

Hamann, F., D. L. Depoy, S. Johansson, and J. Elias: 1994. *Astrophys. J.* **422**, 626–641.

Hillier, D. J., K. Davidson, K. Ishibashi, and T. Gull: 2001. *Astrophys. J.* **553**, 837–860.

Hofmann, K.-H. and G. Weigelt: 1988. *Astron. Astrophys.* **203**, L21.

Hofmann, R., B. Brandl, A. Eckart, F. Eisenhauer, and L. E. Tacconi-Garman: 1995. In: *Proc. SPIE, Infrared Detectors and Instrumentation for Astronomy, Albert M. Fowler; Ed.*, Vol. 2475. pp. 192–202.

Hook, R. N. and L. B. Lucy: 1994. In: *The Restoration of HST Images and Spectra II.* p. 86.

Jones, A. W., J. Bland-Hawthorn, and P. L. Shopbell: 1995. In: *ASP Conf. Ser. 77: Astronomical Data Analysis Software and Systems IV.* p. 503.

Keller, C. U., R. Gschwind, A. Renn, A. Rosselet, and U. P. Wild: 1995. *Astron. Astrophys. Suppl. Ser.* **109**, 383.

KRI: 1996, *Khoros Pro User's Guide.* Albuquerque, USA: Khoros Research, Inc.

Kulagin, E. S.: 1980. *Soviet Astronomy* **24**, 118.

Labeyrie, A.: 1970. *Astron. Astrophys.* **6**, 85.

Lagrange, A., G. Chauvin, T. Fusco, E. Gendron, D. Rouan, M. Hartung, F. Lacombe, D. Mouillet, G. Rousset, P. Drossart, R. Lenzen, C. Moutou, W. Brandner, N. N. Hubin, Y. Clenet, A. Stolte, R. Schoedel, G. Zins, and J. Spyromilio: 2003. In: *Instrument Design and Performance for Optical/Infrared Ground-based Telescopes. Edited by Iye, Masanori; Moorwood, Alan F. M. Proceedings of the SPIE*, Vol. 4841. pp. 860–868.

Lai, O.: 2000. In: *Adaptive Optical Systems Technology, Peter L. Wizinowich ed., Proc. SPIE*, Vol. 4007. p. 773.

Lavalley, C., S. Cabrit, C. Dougados, P. Ferruit, and R. Bacon: 1997. *Astron. Astrophys.* **327**, 671.

le Coarer, E.: 1992. Ph.D. thesis, Université Paris-VII.

le Coarer, E., Y. Georgelin, and J. Boulesteix: 1993. *CFHT Bull.* **29**, 14.

le Coarer, E., Y. Georgelin, and G. Lelièvre: 1992. In: *Progress in Telescope and Instrumentation Technologies.* p. 725.

Le Fevre, O., G. P. Vettolani, D. Maccagni, D. Mancini, J. P. Picat, Y. Mellier, A. Mazure, M. Saisse, J. G. Cuby, B. Delabre, B. Garilli, L. Hill, E. Prieto, L. Arnold, P. Conconi, E. Cascone, E. Mattaini, and C. Voet: 1998. In: *Optical Astronomical Instrumentation, Sandro D'Odorico; Ed., Proc. SPIE*, Vol. 3355. p. 8.

Le Mignant, D., F. Marchis, D. Bonaccini, P. Prado, E. Barrios, R. Tighe, V. Merino, A. Sanchez, The 3. 60m Telescope Team, and ESO Ao Team: 1999. In: *Astronomy with adaptive optics : present results and future programs.* p. 287.

Lucy, L. B.: 1974. *Astron. J.* **79**, 745.

Lucy, L. B.: 1994a. *Reviews of Modern Astronomy* **7**, 31–50.

Lucy, L. B.: 1994b. *Astron. Astrophys.* **289**, 983–994.

Lucy, L. B. and J. R. Walsh: 2003. *Astron. J.* **125**, 2266–2275.

Magain, P., F. Courbin, and S. Sohy: 1998. *Astrophys. J.* **494**, 472.

Maillard, J. P.: 1995. In: *ASP Conf. Ser. 71: IAU Colloq. 149: Tridimensional Optical Spectroscopic Methods in Astrophysics.* p. 316.

Maillard, J. P.: 2000. In: *ASP Conf. Ser. 195: Imaging the Universe in Three Dimensions.* p. 185.

Mariotti, J. M.: 1988. In: *Diffraction-limit.imaging/ Very Large Telescopes, D. Alloin and Mariotti, J.-M., eds, NATO-ASI Series*, Vol. 274. p. 3.

Menard, F., C. Dougados, G. Duchene, J. Bouvier, G. Duvert, C. Lavalley, J. Monin, and J. Beuzit: 2000. In: *Adaptive Optical Systems Technology, Peter L. Wizinowich ed., Proc. SPIE*, Vol. 4007. p. 816.

Mohler, O.: 1955. The The University of Michigan Press: Ann Arbor, 1955.

Perina, J.: 1971. The Modern University Physics Series, London: Van Nostrand, 1971, edited by Conn, G.K.T.

Perryman, M. A. C., A. Peacock, N. Rando, A. van Dordrecht, P. Videler, and C. L. Foden: 1994. In: *ASSL Vol. 187: Frontiers of Space and Ground-Based Astronomy.* p. 537.

Racine, R.: 1996. *PASP* **108**, 699.

Rando, N., A. Peacock, F. Favata, and M. Perryman: 2000. *Experimental Astronomy* **10**, 499.

Rigaut, F., D. Salmon, R. Arsenault, J. Thomas, O. Lai, D. Rouan, J. P. Véran, P. Gigan, D. Crampton, J. M. Fletcher, J. Stilburn, C. Boyer, and P. Jagourel: 1998. *PASP* **110**, 152–164.

Simons, D. A., C. C. Clark, S. S. Smith, J. M. Kerr, S. Massey, and J. Maillard: 1994. In: *Proc. SPIE Vol. 2198, p. 185-193, Instrumentation in Astronomy VIII, David L. Crawford; Eric R. Craine; Eds.*, Vol. 2198. p. 185.

Tikhonov, A. and V. Arsenin: 1977. Washington, DC, USA: Winston.

Titterington, D. M.: 1985. *Astron. Astrophys.* **144**, 381.

Tokovinin, A.: 1992. In: *High-Resolution Imaging by Interferometry.* p. 425.

Trouboul, L., J. Bouvier, A. Chalabaev, and P. Corporon: 1999. In: *Astronomy with adaptive optics: present results and future programs, D. Bonaccini, ed., ESO Conference and Workshop Proceedings*, Vol. 56. p. 681.

Turchin, V. F., V. P. Kozlov, and M. S. Malkevich: 1971. *Sov. Phys. Uspekhi* **13**, 681.

van der Bliek, N. S., J. Manfroid, and P. Bouchet: 1996. *Astron. Astrophys. Suppl. Ser.* **119**, 547.

Weigelt, G. and J. Ebersberger: 1986. *Astron. Astrophys.* **163**, L5.

Weitzel, L., M. Cameron, S. Drapatz, R. Genzel, and A. Krabbe: 1994. *Experimental Astronomy* **3**, 317.

Address for Offprints: e-mail: Almas.Chalabaev@obs.ujf-grenoble.fr